

Article

Low-Cycle Fatigue and Fracture Behavior of Aluminized Stainless Steel AISI 321 for Solar Thermal Power Generation Systems

Wei Li ^{1,2}, Lei Yang ^{1,2,*}, Cong Li ^{1,2,*}, Huitao Chen ^{1,2}, Lu Zuo ^{1,2}, Yide Li ^{1,2}, Jian Chen ^{1,2}, Jianjun He ^{1,2} and Sheng-de Zhang ³

¹ Key Laboratory of Efficient & Clean Energy Utilization, School of Energy and Power Engineering, Changsha University of Science & Technology, Changsha 410114, China; lwzzgjajie@126.com (W.L.); yanglei2630@126.com (L.Y.); chenhuitaocht@126.com (H.C.); zuolu945260417@live.com (L.Z.); m18573160273@126.com (Y.L.); chenjian_513@126.com (J.C.); hejianjun329@126.com (J.H.)

² Department of Smart Grid, Hunan Province 2011 Collaborative Innovation Center of Clean Energy Institute, Changsha 410114, China

³ Japan Electric Power Central Research Institute, Tokyo 240-0196, Japan; hhuang0578@126.com

* Correspondence: liconghntu@csust.edu.cn; Tel.: +86-137-8615-9450

Received: 27 July 2020; Accepted: 10 August 2020; Published: 12 August 2020



Abstract: The microstructure, low-cycle fatigue property, and fracture behavior of as-received and aluminized steel were investigated at room temperature, respectively. The results reveal that the aluminized layer is mainly composed of three layers: (I) the external Al₂O₃ layer, (II) the transition Fe-Al mesophase layer, and (III) the diffusion layer with AlFe and AlCrFe phase. The microhardness of as-received steel lower than that of aluminized steel until the distance from aluminized layer is greater than 150 μm. Compared to the original steel, the aluminized steel exhibits lower stress amplitude and fatigue life, which is correlated to the surface integrity. According to the Coffin-Manson relationship, the fatigue-ductility coefficients for as-received and aluminized steel is 4.347 and 3.528, respectively. Fractographic analysis reveals that the fatigue cracks tend to nucleate at the coating and propagate through the grain boundaries apace.

Keywords: low-cycle fatigue; aluminized steel; surface integrity; fracture behavior

1. Introduction

With the shortage of conventional fossil resource, the innovation of renewable energy sources has been facilitated by the increase of energy consumption unprecedentedly, which has attracted considerable interest [1]. Solar energy, as a major alternative energy sources, takes a large proportion in the total energy of the world [2]. There are two methods used for obtaining the solar energy. One is solar photovoltaic (PV) power generation and the other is concentrated solar thermal power (CSP) [3]. The latter is found to act as an important role in meeting national energy demands and reducing greenhouse gas emissions [4]. With the advantages of being relatively low cost and low emissions, CSP is more suitable to acquire stable dispatchable electrical output as compared to PV-based generation, especially in the application of utility-scale installations larger than 100 MW [5]. However, the interaction of thermal cyclic, mechanical stress and corrosion in heat transfer fluid medium would generate detrimental effect and accelerate the failure of heat exchange tube material [6–9], leading to an increase in the expenditure of maintenance. Therefore, it is very urgent to consider the mechanical strength of the materials as well as their capability against the environmental influence.

AISI 321, a Ti-stabilized grade of austenitic stainless steel, is widely used as vital structural component material in CSP system, such as piping, heat exchangers, and receivers [10–12]. Whereas with

the application of diverse phase transformation heat storage materials, such as molten metal in which stainless steel is corroded seriously, it is inevitable for stainless steel to be refined and meet higher requirements in corrosion resistance. Therefore, it is extremely essential to develop an efficient and reliable coating for the structures of CSP system. $\text{Al}_2\text{O}_3/\text{Fe-Al}$ coating is considered to achieve superior oxidation and corrosion resistance [13]. Different approaches such as chemical vapor deposition (CVD) [14], hot dip aluminizing [15], electrolytic deposition, and pack aluminizing [16] are adopted to prepare the aluminized layer. Among them, pack aluminizing is more prominent due to the cheap price and easy forming with different shapes and sizes [17].

The heat exchange tube material is mainly subjected to low cycle fatigue (LCF) loads under working condition. However, coating microstructure has an important effect on the fatigue performance of the steel. Mušálek R. [18] investigated the influence of Fe-Al coating prepared by plasma spraying on the fatigue behavior of low carbon steel, and found that the fatigue cracks initiated at coating-substrate interface and grew by striation mechanism. Additionally, several authors pointed out that the intrasplat cracking, decohesion, and the poor bonding ability of Al_2O_3 and Fe_3Al would accelerate the fracture of material [19,20]. Furthermore, the surface integrity is of significance to the LCF life. Gun [21] investigated the effects of TiN coating on the fatigue life of AISI D2 tool steel and demonstrated that the fatigue limit was considerably related with the surface integrity. Moreover, many researchers reported that an increased microhardness can improve the LCF life [22–25]. However, there is still a shortage of systematical analyses about the interaction between microstructure and fatigue behavior in aluminized steel. Therefore, the microstructural evolution of aluminide coating and its effects on the LCF property are studied in this paper. The paper is organized as follows. Section 2, after the aluminized steel is prepared, static tensile and LCF tests are conducted at room temperature. Subsequently, the microstructure, tensile property, surface integrity, hysteresis loops, cyclic stress response, and LCF life of aluminized steel are presented and compared with base metal in Section 3. In the same section, the fatigue fractographic of these materials were observed using scanning electron microscopy (SEM). In Section 4, the microstructure evolutions during pack aluminizing are discussed. Finally, the effective fatigue stress concentration and the degree of hardening for both steel are calculated.

2. Materials and Methods

The nominal compositions of the stainless-steel (grade AISI 321) are shown in Table 1. Test specimens were cut from the as-received slab and ground to 2000-grit SiC paper. They were rinsed with ethanol, and dried before aluminizing. Pieces of samples were completely embedded in the aluminizing agent, which is composed of 68 wt. % Fe-Al powder, 30 wt. % Al_2O_3 filler, and 2 wt. % NH_4Cl activator, and then filled into a heat-proof stainless-steel container. The container was heated to 500 °C for 30 min primarily, and then elevated to 950 °C for 12 h at a heating rate of 10 °C/min, finally cooled to the room temperature in the air.

Table 1. Chemical composition of 321 austenitic stainless steels.

Element	C	Si	Mn	P	S	Cr	Ni	N	Ti
wt. %	0.035	0.38	1.08	0.028	0.003	17.02	9.06	0.045	0.22

All mechanical tests were performed on RDL05 electronic creep fatigue testing machine (Changchun Research Institute for Testing Machines, Changchun, China), equipped with 50 KN load cell. Static tensile tests and LCF tests were conducted at room temperature, using samples of 25 mm gauge length and 4 mm × 8 mm sectional dimension as shown in Figure 1. Tensile tests were implemented at a strain rate of 10^{-3} s^{-1} . LCF tests were carried out at a constant cyclic frequency of 0.2 Hz and the load ratio was $R = -1$. LCF tests were performed at total strain amplitudes of 0.3–0.8%. All strain was measured by mounting extensometer.

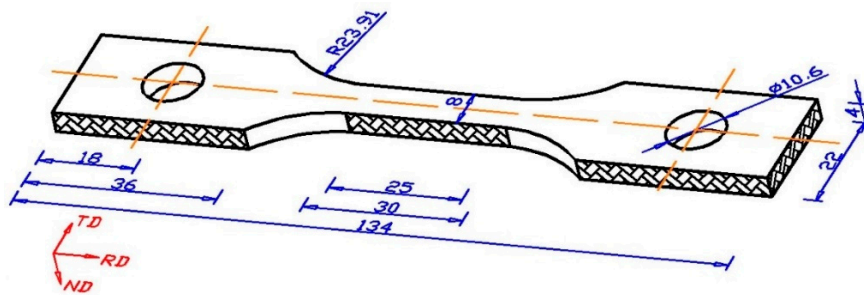


Figure 1. Schematic diagram of samples for tensile and fatigue tests, mm.

The aluminized coatings were characterized by A TD3000 X-ray diffractometer (XRD, Dandong Tongda Technology Co. Ltd, Dandong, China). The surface roughness was measured by JB-4C precision roughness tester and 3D surface profiles were observed through the VHX-1000 super-deep 3D microscopic system (Yalieu Institute of Mechanical and Electrical Technology, Beijing, China). The micro-hardness was tested with a 410MVA Vickers micro-hardness tester (Laizhou Huayin Institute for Testing Instrument, Laizhou, China) using a load of 300 g and hold time of 15 s. Fracture surfaces of the fatigue tested samples were examined by Quanta 2000 environment SEM (FEI, Hillsboro, OR, USA).

3. Results

3.1. Microstructure Characterization and Tensile Property

Typical SEM images of surface and cross-section of aluminized steel are shown in Figure 2a,b, respectively. It can be seen from Figure 2a that the grain with size of 3–5 μm distributes uniformly while the Al_2O_3 distributes at random upon the surface of coating, which increases the surface roughness seriously. As can be seen in Figure 2b, the aluminizing coating has a multi-layer structure. According to the EDS analysis listed in Table 2, the coating structure can be classified into a top discontinuous Al_2O_3 (region I), followed by a Fe-Al transition layer of 15 μm (region II) and finally a AlCrFe diffusion layer of 75–80 μm (region III). It is worth noting that there exists a mixed of cross shape precipitation and microcracks in region III, which is consistent with the observations in Reference [26]. X-ray diffraction diagram of Fe-Al transition layer is shown in Figure 3. The XRD test result indicates that austenite is dominant in stainless steel; however, the Fe-Al transition layer includes Fe_3Al , FeAl , and FeAl_2 phases with different proportions. In particular, there is a brittle phase (FeAl_3) containing higher aluminum content, leading to the nucleation of tiny cracks.

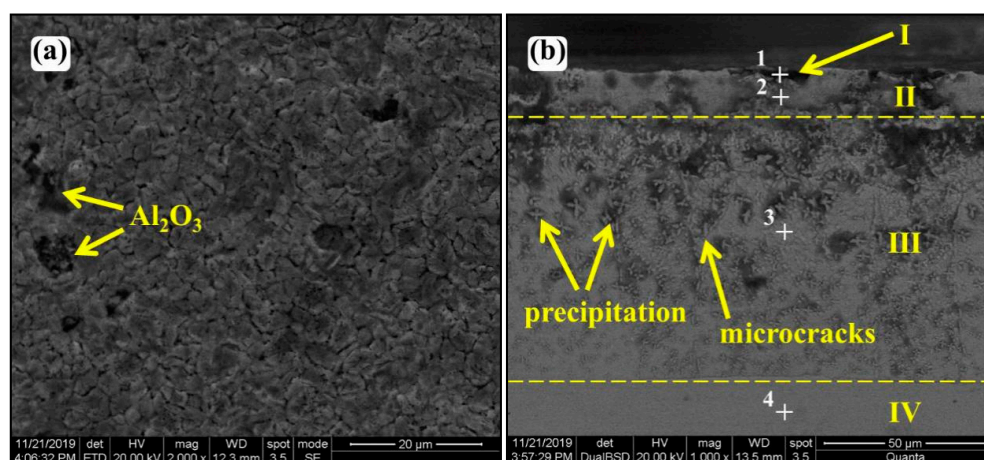


Figure 2. Scanning electron microscopy (SEM) of aluminized 321 stainless steel: (a) surface; (b) cross-section.

Table 2. Energy dispersive spectrometer (EDS) analysis of different regions in aluminized coating (white points in Figure 2b), (at. %).

Point	Fe	Al	O	Cr
1 (external layer)	0.44	32.45	59.89	4.72
2	30.68	43.98	15.21	7.01
3	50.01	23.54	3.33	9.38
4	76.62	1.40	0	17.49

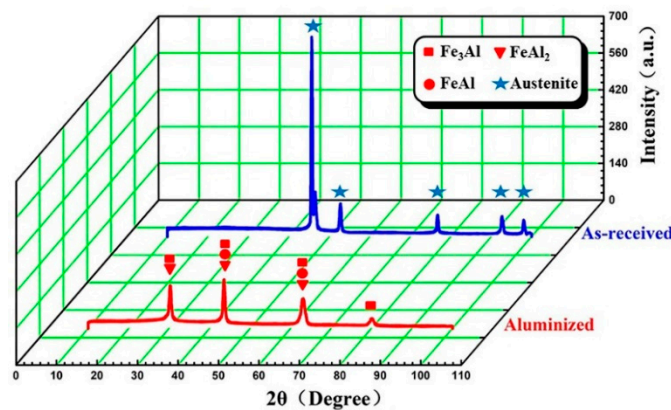


Figure 3. X-ray diffractometer (XRD) data of as-received steel and aluminized steel.

The tensile engineering stress-strain curves and fracture surfaces are exhibited in Figure 4. As can be seen, the fracture surfaces of as-received steel (surrounded by blue frame) includes dimples and voids, while cleavage planes are observed in the fracture surfaces of aluminized steel (surrounded by red frame). This indicates a deterioration on ductility of stainless steels after aluminized. The mechanical properties of as-received and aluminized steel measured at room temperature (30 °C) are summarized in Table 3. The yield strength (σ_{ys}) is defined as the stress corresponding to a plastic strain of 0.2%. It can be found that the aluminizing process has decreased the elongation (A) and ultimate tensile strength (σ_b) by 19.0% and 14.8%, but its σ_{ys} deterioration is relatively small. Furthermore, the difference between the σ_{ys} and σ_b indicates the degree of working hardening of materials during monotonic deformation. In this aspect, the working hardening of as-received samples is stronger than that of aluminized samples, which is attributed to the surface integrity and phase transformation during aluminizing. Therefore, these results reveal that as-received steel has better strength and higher ductility as compared to the aluminized steel.

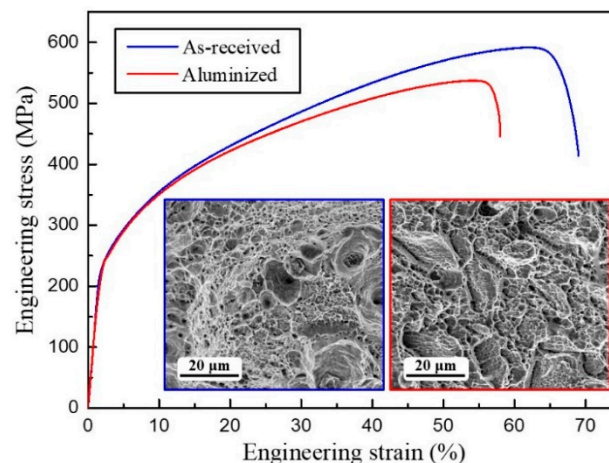


Figure 4. Engineering stress-strain curves and fracture surfaces of as-received steel and aluminized steel.

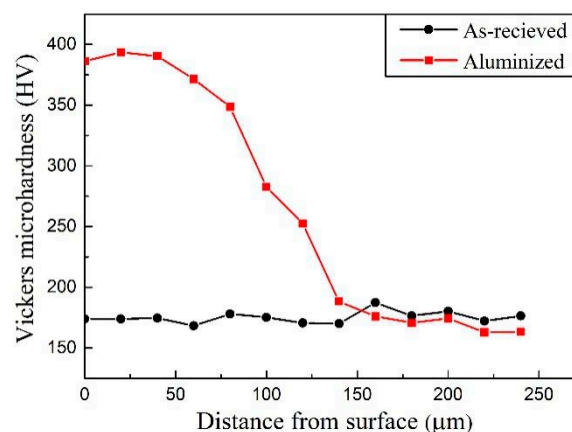
Table 3. Room-temperature mechanical properties of aluminized and as-received steel.

Samples	0.2% Yield Strength (σ_{ys}) (MPa)	Ultimate Tensile Strength (σ_b) (MPa)	Elongation (A) (%)
As-received	260	608	69
Aluminized	232	518	58

3.2. Surface Integrity

3.2.1. Microhardness

The microhardness of the as-received and aluminized specimens was measured along the vertical depth of aluminized layer, as shown in Figure 5. Basically, the Vickers microhardness of the as-received sample is around 175 HV. For the aluminized grade, the microhardness is up to 380 HV on the outmost of the aluminized surface consequently reaches the highest value about 390 HV at the 25 μm distance from the surface, then exhibits a decrease with the increasing distance from the aluminized layer. In addition, the microhardness of as-received steel does not exceed that of aluminized steel until the distance from aluminized layer is greater than 150 μm . It can be supposed that there is a direct correlation between the amount of aluminum and the corresponding microhardness value. In other words, microhardness value is in proportion to the aluminum concentration, which has been mentioned in several studies [16,27]. Besides, it is also shown that obscure softening occurs at the substrate, which may be relevant to the precipitation of solid solution.

**Figure 5.** Microhardness variation along the depth of samples.

3.2.2. Surface Roughness

As one of the most significant parameters of surface geometrical characteristics, surface roughness has a great influence on the fatigue performance of materials. Normally, the surface roughness is evaluated by peak-to-valley height (R_y), contour-calculated average deviation (R_a), and 10-point surface height (R_z), where R_a can reflect both the microscopic geometric features and the height of convex peak, whereas R_z describes the limit of surface roughness [28]. All of these values are listed in Table 4. Figure 6 displays 3D surface profile for both materials. The parameter X represents the vertical distance from a specific point to the lowest valley within the visible region. Figure 6 implies that the surface of the as-received sample is smoother and flatter than that of the aluminized sample. The dimples on the surface of the as-received sample are more regular, which corresponds to the value of R_a .

Table 4. Surface roughness for samples in the condition of as-received steel and aluminized steel.

Sample	R_a (μm)	R_z (μm)	R_y (μm)
As-received	0.168	0.962	1.97
Aluminized	0.952	7.174	9.473

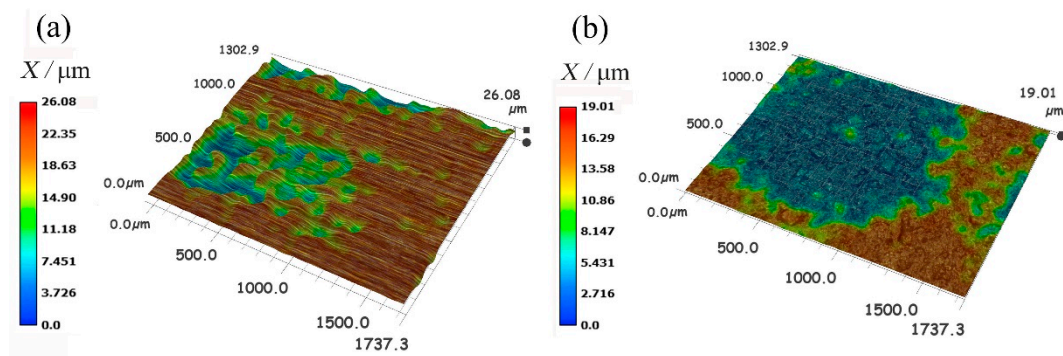


Figure 6. 3D surface profile of (a) as-received steel and (b) aluminized steel.

3.3. Hysteresis Loops and Cyclic Stress Response

Figure 7 displays the hysteresis loop for the first cycle and half-life of both steel with a series of strain amplitudes during LCF loading. In terms of as-received steel (Figure 7a–d), the difference between the maximum tensile stress and the maximum compressive stress is not conspicuous. Additionally, the stress amplitude of the half-life is greater than that of the first cycle, indicating that a hardening occurs in the process of LCF. Moreover, the hardening degree of as-received steel increases with the strain amplitude, which is further discussed in Section 4.3. As can be seen from Figure 7e–h, a similar trend has been observed in aluminized steel except that the maximum compressive stress is greater than the maximum tensile stress for the same materials during LCF. However, it is worth noting that when the strain amplitude reaches 0.7% (Figure 7h), the hysteresis loop of aluminized steel gets unstable as compared to that under other strain amplitude. This is attributed to the influence of the coatings.

The CSR curves under different total-strain amplitude are described in Figure 8a,b. It can be observed from Figure 8a that the CSR curves of as-received steel basically exhibits regions of initial hardening followed by cyclic saturation and secondary hardening before the stress dropped dramatically relevant to the propagation of cracks nucleated at the periphery of specimens at the strain amplitudes 0.3–0.8%. Similar tendency in cyclic stress response is also observed in aluminized steel at the strain amplitude of 0.6–0.7% (as shown in Figure 8b). However, at the strain amplitude of 0.3–0.4%, aluminized steel displays initial hardening followed by a cyclic saturation, subsequently slight softening and then secondary hardening. On the other hand, the initial hardening rate of aluminized steel is greater than that of as-received steel at the same strain amplitude. All materials have experienced rapid secondary cyclic hardening, which might be contributed to martensitic transformation [29]. Hardening, at the primary stage of cycle deformation, is deemed to be mainly caused by the dislocation proliferation. Nevertheless, secondary cyclic hardening occurs after a certain incubation period (about 5000 cycles at 0.3% in Figure 8a). Similar observation has been documented by Prasad Reddy et al. [30], who pointed out that increase in strain amplitude leads to a transition from planar slip bands to dislocation cell or dislocation wall structure. In particular, the stress amplitudes of aluminized steel are commonly lower than 321 stainless steel at the same strain amplitude, which is attributed to the microstructure of aluminized coating.

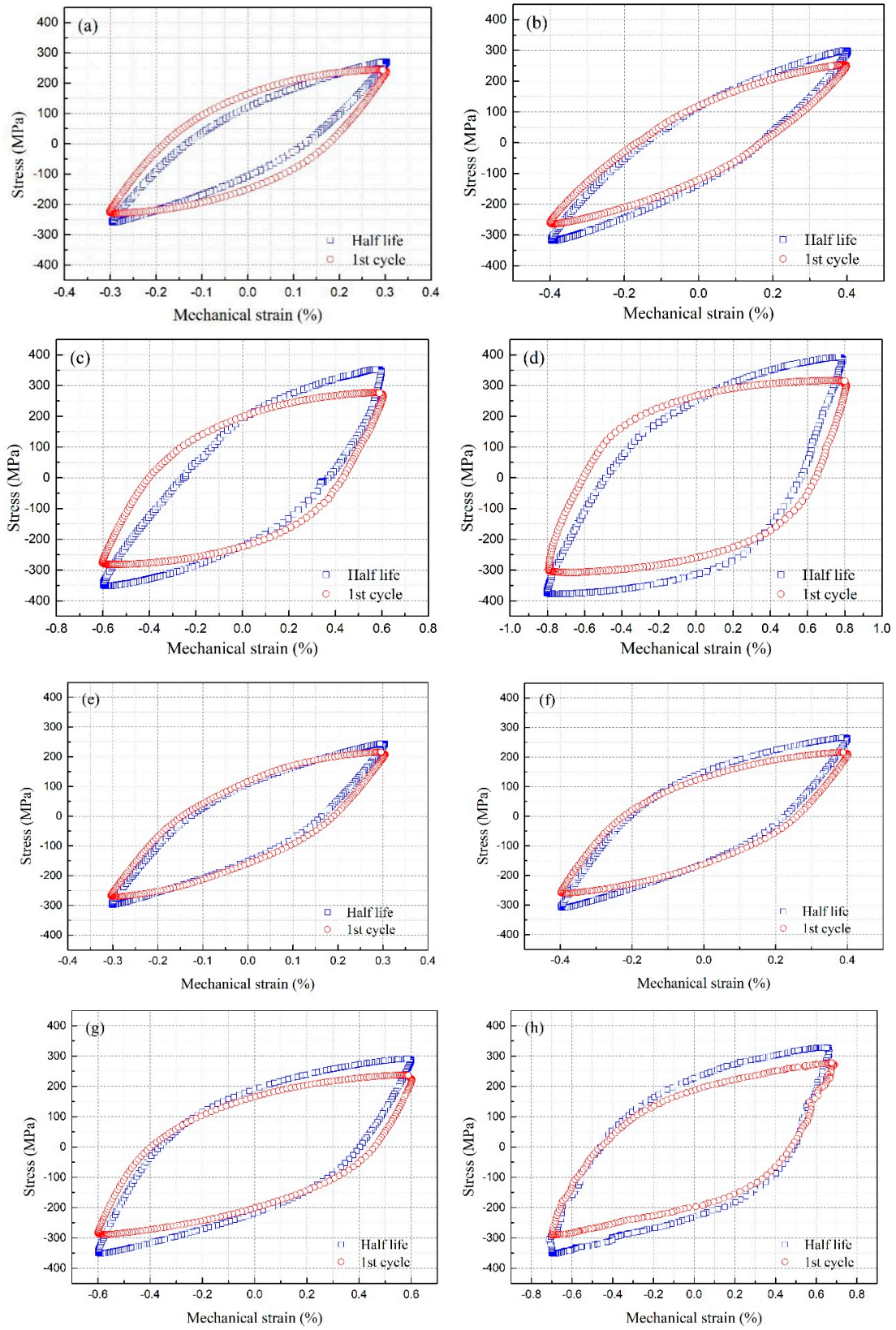


Figure 7. Stress-mechanical strain hysteresis loops of as-received steel: (a) 0.3%; (b) 0.4%; (c) 0.6%; (d) 0.8%; and aluminized steel: (e) 0.3%; (f) 0.4%; (g) 0.6%; (h) 0.7%.

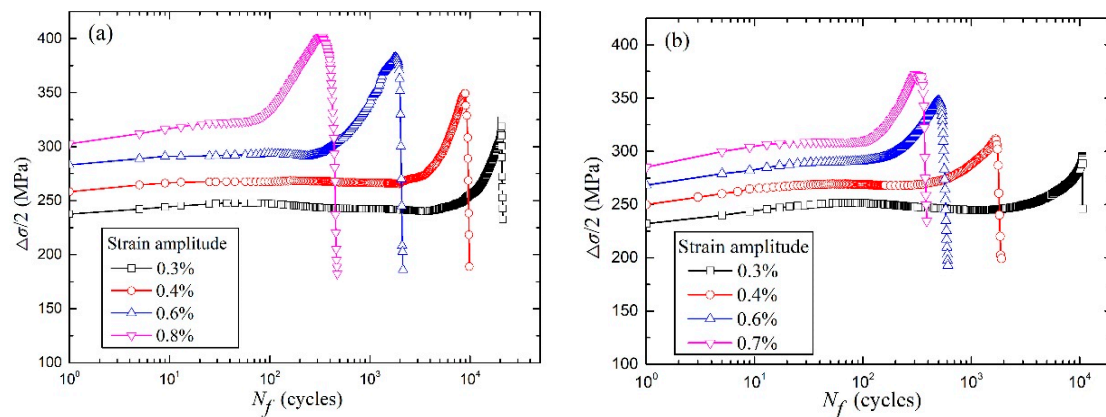


Figure 8. Cyclic stress response curve for (a) as-received sample; (b) aluminized sample.

3.4. Low-Cycle Fatigue Life

LCF fatigue tests results are listed in Table 5. The table includes the total strain amplitudes (ε_t), plastic strain amplitudes (ε_p), elastic strain amplitudes (ε_e), and the resulting number of cycles to failure (N_f) for each specimen. The hysteresis loops at half-life are used to determine ε_p . The variation of fatigue life, in terms of number of reversals to failure ($2N_f$), with ε_e , ε_p , and ε_t is calculated respectively on the equation of the strain-life relationship explored by Basquin and Coffin-Manson [31], which can be expressed as

$$\varepsilon_t = \varepsilon_e + \varepsilon_p = \frac{\sigma'_f}{E}(2N_f)^b + \varepsilon'_f(2N_f)^c \quad (1)$$

where σ'_f is the fatigue strength coefficient, b is the fatigue strength exponent, ε'_f is the fatigue ductility coefficient, and c is the fatigue ductility exponent.

Table 5. Summary of LCF fatigue tests results.

Sample	$\Delta\varepsilon_t/2$ (%)	$\Delta\varepsilon_p/2$ (%)	$\Delta\varepsilon_e/2$ (%)	N_f
As-received	0.3	0.12822	0.17178	20632
As-received	0.4	0.15674	0.24326	9918
As-received	0.6	0.31116	0.28884	2324
As-received	0.8	0.52592	0.27408	338
Aluminized	0.3	0.14535	0.15465	10685
Aluminized	0.4	0.21578	0.18422	1923
Aluminized	0.6	0.38358	0.21642	635
Aluminized	0.7	0.48018	0.21982	325

The data of ε_t , ε_e , ε_p , and $2N_f$ are plotted on a bilogarithmic scale in Figure 9. It is observed that the elastic strain amplitude takes an essential portion of the total strain amplitude in both steels. The linear relationship on a log-log plot of both elastic and plastic strain amplitude indicates that Equation (1) can be applied to determine the fatigue behavior. The fatigue ductility exponents (c) for 321 stainless steel and aluminized steel are -0.355 and -0.351 , respectively. While the fatigue ductility coefficient (ε'_f) is 4.347 for 321 stainless steel and 3.528 for aluminized steel, which is consistent with the rules of monotonic ductility and suggests that the aluminized stainless steel is less durable than 321 stainless steel. The same results have also been reported by Duyi Ye et al. [32]. In the present study, it is explained that the inferior cyclic ductility of the aluminized steel is probably attributed to local stress concentration on the tough coating and deformation features of the microstructure of steel during aluminizing process and fully reversed cyclic straining.

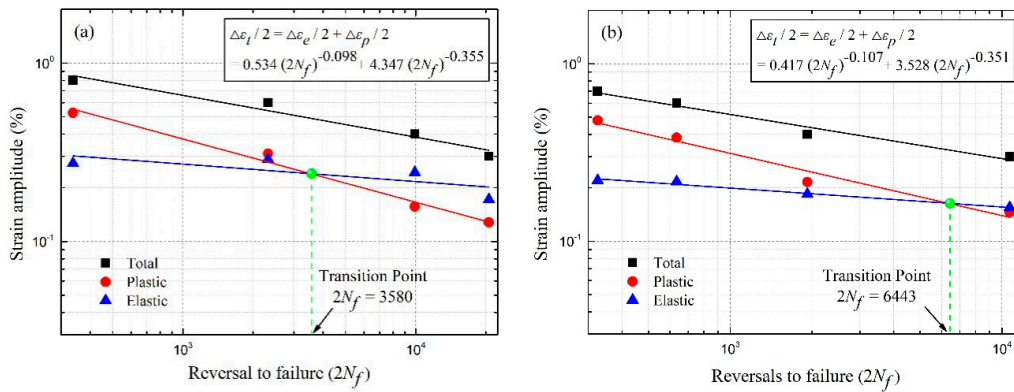


Figure 9. Strain amplitude vs. reversals to failure curves for (a) as-received sample; (b) aluminized sample.

3.5. Fracture Behavior

Figure 10 displays typical SEM fracture surface of fatigue-failed specimens at strain amplitudes of 0.3%. It can be seen that both as-received and aluminized specimens exhibit crack initiation zone, propagation zone, and final fracture zone (Figure 10a,e). As is evidence in Figure 10a, there are several inclusions in crack initiation zone, around which microcracks nucleate and spread radially. The inclusion-type nucleation can be explained as cyclic slip localization reinforced by stress-concentration [33]. Higher magnified observation of the crack initiation region (Figure 10b) shows that crack branching with different directions originated along with grain boundaries and the microcracks generates from the cross point of the cracks. However, widely spaced striations joined by tear ridges have been observed in the propagation area of as-received steel (Figure 10c), which implies a low rate of crack propagation. Figure 10d magnifies the final fracture zone, revealing that the existence of the large dimple is usually relevant to inclusions or the secondary phase particles.

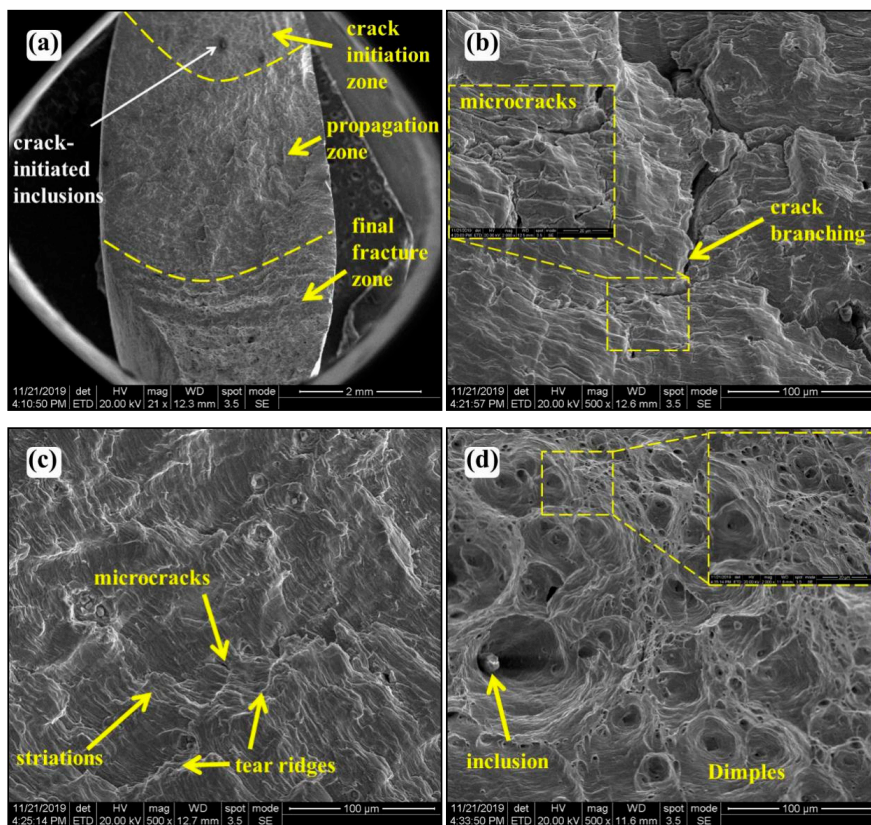


Figure 10. Cont.

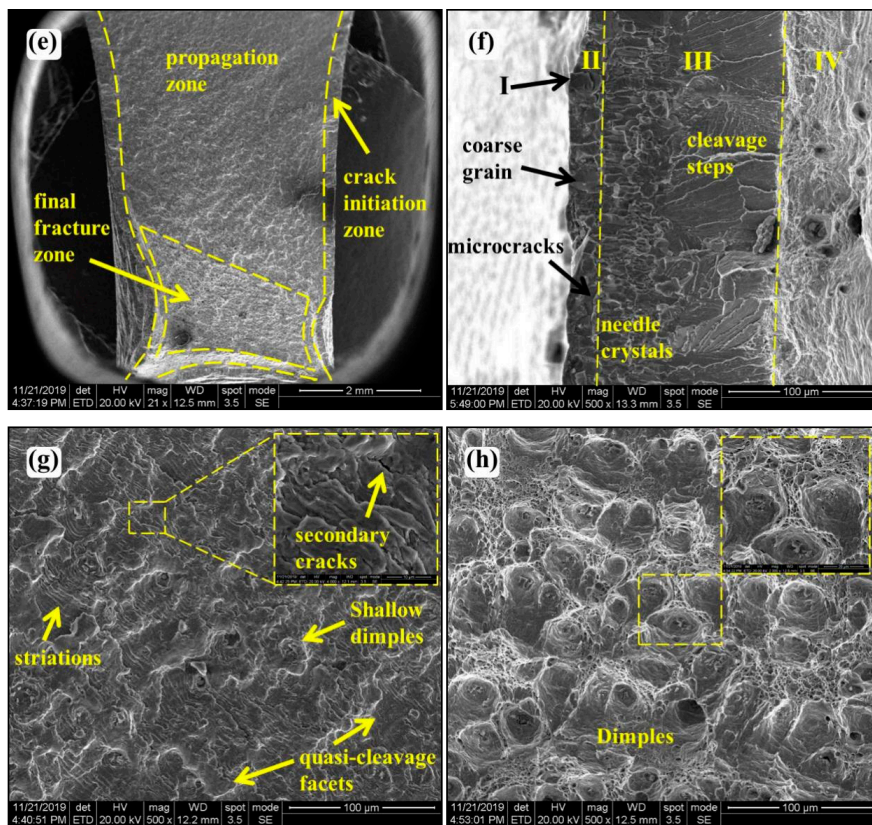


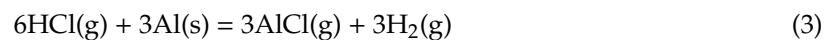
Figure 10. SEM micrograph of low-cycle fatigue morphology at the strain amplitude of 0.3%: (a) the global view of as-received steel; (b) crack initiation zone of as-received steel; (c) crack propagation zone of as-received steel; (d) final fracture zone of as-received steel; (e) the global view of aluminized steel; (f) crack initiation zone of aluminized steel; (g) crack propagation zone of aluminized steel; (h) final fracture zone of aluminized steel.

In aluminized steel, the crack propagation zone constituted 60% of the area and the microcracks nucleated on the surface of the coatings (Figure 10e) extend into the substrate rapidly. Accordingly, the crack initiation area of aluminized steel (Figure 10f) presents a layered construction in correspondence with Figure 2b. Conspicuously, Al_2O_3 is prone to peel off during low cycle fatigue test because of the brittleness of Al_2O_3 (layer I). In addition, the Fe-Al transition layer (layer II) is characterized by coarse grain, at which intergranular cracks originate and extend through the grain boundary to subsequent internal layers. Nevertheless, Fe(Al) diffusion layer (layer III) displays two types of morphologies. Put another way, needle crystals locate near to Fe-Al transition layer and cleavage steps remain close to the substrate, which is ascribed to the rearrangement of dislocation against fatigue stress for the duration of LCF. Aluminized steel (Figure 10g) exhibits a brittle fracture mode in the propagation region, typified by quasi-cleavage facets, striations, and shallow dimples. The transgranular crack expansion is responsible for the nucleation of secondary crack hiding in striations at the top right corner [33]. In comparison with as-received steel (Figure 10c), the striation is denser and the microcrack is narrower in aluminized steel. This is because the lower plastic deformation resistance is the most likely the major reason for the degradation of abilities against cycle loading, which brings about rapid crack growth rates and accelerates the failure of material dramatically. After aluminizing, dimples described in Figure 10h become more uniform and are raised in density.

4. Discussion

4.1. Microstructure Evolution

Since the aluminum particles in aluminizing agent are surrounded by aluminum oxide, the Al atoms cannot permeate into the substrate directly except for the activation treatment by activator NH_4Cl . Thus the reactions involved in pack cementation is comprised of the generation of active aluminum atoms [Al] and the production of iron-aluminum alloy phases attached on the substrate. In the first step, NH_4Cl resolves into two types of gases at elevated temperature, one of which reacts with Fe-Al powders to create Al chlorides gaseous precursors. The reactions taking place across the powder-substrate interface are shown as



In these equations, AlCl acts as a transporter who releases the activated [Al] to the substrate surface after collecting Al atoms from aluminizing agent. Additionally, the thermodynamic activities of the alloy elements such as Al and Fe in the agent exceed their activities at the substrate surface, providing an gradient to drive force for gas phase (AlCl) diffusion from the powder to the substrate surface. In the second step, [Al] diffuses into stainless steel ceaselessly while Fe atoms in the substrate move to the surface of stainless steel. With adequate migration proportion and duration, solid solutions formed by Al atoms dissolving in Fe crystal lattices grow into Fe-Al intermetallic compound and develop to aluminizing coatings eventually. Researchers [16] reported that the composition of aluminized coating, to a large extent, was influenced by temperature and duration, indicating that the fatigue properties of aluminized steel was controlled by aluminizing parameters fundamentally. In general, the aluminizing coating include Fe_2Al_5 phase mainly forms at the temperature from 500 °C to 600 °C, while Fe_3Al phase is predominant at the temperature higher than 900 °C [17]. However, FeAl_2 , as a metastable structure, is transformed to other Fe-Al intermetallic phase with the change of temperature [34]. In present study, the aluminizing temperature is 950 °C and the coating contains FeAl, FeAl_2 , and Fe_3Al . Both FeAl and Fe_3Al represent good strength and ductility at room temperature, which inhibits obvious gap in the cyclic loading across the coating-substrate interface.

It has been investigated that the stabilization of Ti cannot guarantee to prevent the intergranular corrosion, which can be induced by Cr depletion due to segregation of Cr in the vicinity of intergranular TiC precipitates and result in severe loss of corrosion resistance, strength, and ductility [35]. The treating temperature (950 °C) is lower than solution temperature. Therefore, the heat treatment becomes an accelerator to stimulate the activation of elements in the substrate, leading to M_{23}C_6 carbides precipitating along the grain boundaries. Simultaneously, the formation of intermetallic phases, such as sigma phase, is a serious problem for austenite stainless steel at elevated temperature [36]. In the present study, both the influence of aluminized coating on the surface and the microstructure changes in the substrate are responsible for the truth that the ductility of aluminized steel is slightly lower than as-received steel.

4.2. Surface Integrity

Hardness analysis is a quantitative method to determine the strength of different materials by measuring the size of indent [24]. As the formation of Fe-Al intermetallic compounds, aluminized coating has excellent microhardness as compared to substrate apparently. Therefore, some performances of aluminized surface—such as abrasive resistance, oxidation resistance, and corrosion resistance—are improved greatly. Nevertheless, in terms of aluminized steel, the fatigue life decreased by 50% at the strain amplitude of 0.3% with the increasing microhardness of aluminide layer. It is associated with

the composition and characteristics of aluminide layer. As observed in Figure 5, Fe-Al intermetallic compound is harder than 321 stainless steel, which have been mentioned in literatures [16,37]. Moreover, the main reason is that there exist uneven Al_2O_3 film on the aluminide surface leading to crack initiating easily. Thus the crack initiation of aluminized steel is related to the defects on the surface predominantly, which can be measured by the surface roughness. Additionally, the substrate becomes relatively softer after aluminizing, which decreases fatigue life by further accelerating the crack propagation.

Results from fatigue testing of as-received sample and aluminized sample elucidate that a decrease in fatigue life occurs with the increase of surface roughness because of the stress concentration. The relationship of the stress concentration and the surface roughness has been studied by Arola [28] and Peterson [38]. The effective fatigue stress concentration factors of machined surface were generally determined by the Arola-Ramulu model [28] and Neuber rule [39]. Recently, an alternative expression for the stress concentration imposed by surface texture has been put forward according to Neuber rule [39]. The effective stress concentration (\bar{K}_t) for the process-dependent surface texture is defined with dominant profile valleys and the corresponding average valley radii. The ultimate expression for \bar{K}_t represented on the basis of standard roughness parameters is written as

$$\bar{K}_t = 1 + n \left(\frac{R_a}{\bar{\rho}} \right) \left(\frac{R_y}{R_z} \right) \quad (5)$$

where R_a , R_y , and R_z are the average roughness, peak-to-valley height, and 10-point roughness as described in Equation (5). The parameter $\bar{\rho}$ is the effective profile valley radius and represents the average radius determined from the dominant profile valleys. While n is an empirical constant, depending on materials and load types. Similar to Neuber rule, $n = 1$ for shear loads and $n = 2$ for uniform tension.

In terms of Peterson [38], the effective fatigue stress concentration \bar{K}_f can be described as

$$\bar{K}_f = 1 + q(\bar{K}_t - 1) \quad (6)$$

where q is the notch sensitivity, relating to the material and asperities geometry. It can be defined by the effective profile valley radius ($\bar{\rho}$) of the surface texture replacing the signal notch root radius (ρ) [39]

$$q = \frac{1}{(1 + \gamma/\bar{\rho})} \quad (7)$$

where γ is a material constant in terms of the ultimate strength (σ_b) for steels

$$\gamma = 0.025 \left(\frac{2070 \text{MPa}}{\sigma_b} \right)^{1.8} \text{ mm} \quad (8)$$

According to 2D surface texture (Figure 11), the effective profile valley radii ($\bar{\rho}$) can be calculated by the average value of at least three critical profile valley radii. The value of $\bar{\rho}$ is 0.107 and 0.210 for 321 stainless steel and aluminized steel, respectively. The statistics about ultimate strength and roughness of materials from Tables 3 and 4 can be substituted into Equation (8) and Equation (5) respectively for getting the value of γ and \bar{K}_t , also q and \bar{K}_f can be deduced from Equation (7) and Equation (6).

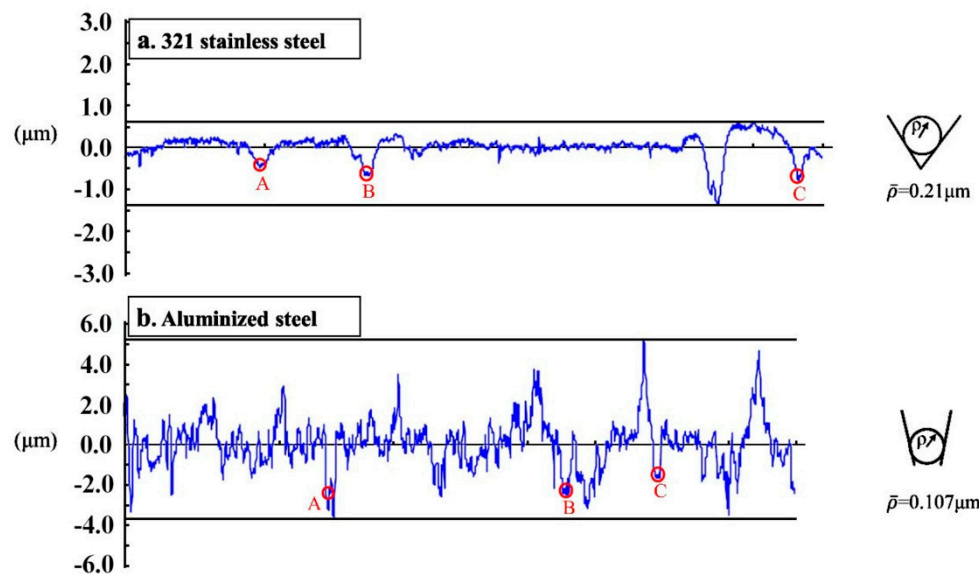


Figure 11. 2D surface texture and effective profile valley radii of (a) as-received sample and (b) aluminized sample.

Table 6 shows derivation statistics for both materials. It can be observed the value of \bar{K}_f in aluminized steel is slightly higher than that in 321 stainless steel due to the small difference of the ultimate strength (σ_b). However, the \bar{K}_t value of as-received steel is much lower. Microscopic observation clearly indicated that fatigue failure of aluminized steel initiated at surface defects, such as pores or Al_2O_3 film. These defects coarsen the surface of aluminized steel greatly and the stress concentration turns to be more intense, leading to rapid crack initiation. Once they initiate and expand from the surface, the cracks would not be interrupted to propagate along the grain boundaries of Fe-Al intermetallic compound into subsequent inner layers until the final failure.

Table 6. Derivation statistics for as-received sample and aluminized sample.

Sample	σ_b (MPa)	$\bar{\rho}$ (μm)	γ (mm)	q	\bar{K}_t	\bar{K}_f
As-received	608	0.210	0.227	0.000925	4.286	1.003
Aluminized	518	0.107	0.303	0.000353	24.497	1.008

4.3. Cyclic Stress Response

For the purpose of describing cycle hardening as a function of total strain amplitudes (ε_t) and comparing the relative magnitude, the degree of hardening (H) has been defined as [40]

$$H = \frac{\sigma_{N/2} - \sigma_1}{\sigma_1} \quad (9)$$

where σ_1 and $\sigma_{N/2}$ represent the stress range at the first cycle and half-life, respectively. The linear dependence between H and ε_t has been simulated in Figure 12, in which a conspicuous increment could be found in as-received steel, raising from 0.0806 to 0.2397 with ε_t increasing from 0.3% to 0.8%. Similar trend has been observed in aluminized steel. Meanwhile, at low strain amplitudes (0.3% and 0.4%), the degree of hardening in as-received steel is lower than that in aluminized steel. However, at high strain amplitudes ($\geq 0.6\%$), the hardening effect of as-received steel is much higher than that of aluminized steel.

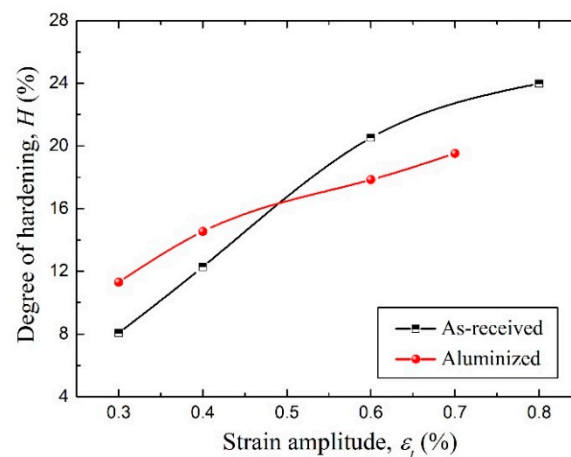


Figure 12. Dependence of the degree of cyclic hardening on imposed strain amplitude.

Kim [41] pointed out that in the establishment of internal-diffusion barrier, the sigma phase driven by solid solution strengthen was stable enough to be detected in substrate during the whole aluminizing process at temperatures below 1000 °C. On the one hand, sigma phase would block the dislocation mobility among the grains and inhibit the slip of grain boundary in substrate leading to dislocation tangle existing around the sigma phase and local hardening, which is, in some conditions, the causes that at low strain amplitudes (0.3% or 0.4%), the degree of hardening in as-received steel was lower than that in aluminized steel exhibited in Figure 12. On the other hand, the bonding strength produced by the brittle sigma phase among austenite particles is too delicate to suppress secondary crack initiation, which would degrade the plasticity of the material greatly [42]. Additionally, brittle phases forming in coating such as FeAl_2 act as chief criminal to accelerate the initiation and propagation of microcracks. Thereby, as-received steel greatly exceeded aluminized steel in the degree of hardening at high strain amplitudes ($\geq 0.6\%$).

However, other authors found that the formation of sigma phase requires high-energy interfaces, such as large-angle grain boundaries or the second phase (oxidation) and quite long aging time (several 10 thousand hours) [42]. Not only does M_{23}C_6 carbide offer an attachable site for cavity nucleation [43] but leads to grain boundary serration [44]. Accordingly, the deterioration of stress amplitude in aluminized steel could attribute to the cooperative influence between M_{23}C_6 and sigma phase produced in the aluminizing process predominantly.

5. Conclusions

In this study, the low cycle fatigue properties of 321 stainless steel with pack-aluminized treatment were investigated. The influence of aluminizing coating on the low cycle fatigue performance was analyzed through comparing the microstructural characteristics and surface integrity. The main findings are summarized below:

(1) The aluminized layer is mainly composed of three layers: (I) the external Al_2O_3 layer, (II) the transition Fe-Al mesophase (such as Fe_3Al , FeAl , FeAl_2) layer, and (III) the diffusion layer with AlFe and AlCrFe phase.

(2) The microhardness of as-received steel is lower than that of aluminized steel until the distance from aluminized layer is greater than 150 μm . Additionally, the surface of as-received sample is smoother than that of aluminized sample. The exterior hardening and embrittlement, as well as interior softening, accelerate the propagation of cracks.

(3) Regions of initial hardening, subsequent saturation, and (or a slight softening) the secondary cyclic hardening are represented in CSR. Whereas the stress amplitude of aluminized steel is inferior to that of 321 stainless steel with the same strain amplitude.

(4) LCF data of aluminized steel and 321 stainless steel is in agreement with Coffin-Manson relationship. The fatigue-ductility coefficient of aluminized steel ($\epsilon'_f = 3.528$) is lower than that of 321 stainless steel ($\epsilon'_f = 4.347$), implying a shorter fatigue life in aluminized steel. Fracture analysis of aluminized steel reveals that fatigue crack is prone to nucleate at the aluminized coating and propagates along the grain boundaries of the Fe-Al transition layer.

Author Contributions: W.L. and C.L. designed the research project and wrote the manuscript; L.Y. and Y.L. performed the experiments; H.C., L.Z., J.C., J.H., and S.-d.Z. analyzed the data. All authors have read and agreed to the published version of the manuscript.

Funding: The authors received financial support of the National Natural Science Foundation of China (No. 51675058), Research Foundation of Education Bureau of Hunan Province (Grant No. 19B033), the science and technology innovation project of Hunan Province (No. 2018RS3073) and the Natural Science Foundation of Hunan Province (No. 2018JJ3531, 2018JJ3539), the double first-class scientific research international cooperation project of Changsha university of science and technology (2019IC15), Scientific research innovation Project for Graduate student of Hunan province (No. CX2018B560).

Conflicts of Interest: The authors declare no conflict of interest.

References

1. Regin, A.F.; Solanki, S.C.; Saini, J.S. Heat transfer characteristics of thermal energy storage system using PCM capsules: A review. *Renew. Sustain. Energy Rev.* **2008**, *12*, 2438–2458. [\[CrossRef\]](#)
2. Xu, B.; Li, P.; Chan, C. Application of phase change materials for thermal energy storage in concentrated solar thermal power plants: A review to recent developments. *Appl. Energy* **2015**, *160*, 286–307. [\[CrossRef\]](#)
3. Py, X.; Azoumah, Y.; Olives, R. Concentrated solar power: Current technologies, major innovative issues and applicability to West African countries. *Renew. Sustain. Energy Rev.* **2013**, *18*, 306–315. [\[CrossRef\]](#)
4. Wang, Z. Prospectives for China's solar thermal power technology development. *Energy* **2010**, *35*, 4417–4420. [\[CrossRef\]](#)
5. Christopher, C.; Benjamin, K.S. Miracle or mirage? The promise and peril of desert energy part 1. *Renew. Energy* **2013**, *50*, 628–636.
6. Vignarooban, K.; Xu, X.; Arvay, A.; Hsu, K.; Kannan, A.M. Heat transfer fluids for concentrating solar power systems—A review. *Appl. Energy* **2015**, *146*, 383–396. [\[CrossRef\]](#)
7. Junping, J.; Hua, T.; Peng, J. Economic potential to develop concentrating solar power in China: A provincial assessment. *Renew. Sustain. Energy Rev.* **2019**, *114*, 109279.
8. Xiao, H.; Xie, P.; Cheng, M.; Song, L. Enhancing mechanical properties of quasi-continuous-wave laser additive manufactured Inconel 718 through controlling the niobium-rich precipitates. *Addit. Manuf.* **2020**, *34*, 101278.
9. Stéphanie, G.; Abdessamad, F.; Aydar, R.; Julien, L.; Emmanuel, V.; Patrick, E.; Catherine, B.; Nicolas, C.; Py, X. Corrosion effects between molten salts and thermal storage material for concentrated solar power plants. *Appl. Energy* **2012**, *94*, 174–181.
10. Smola, B. Precipitation and hardening mechanisms in the AISI 321 steel. *Acta Univ. Carolinae. Math. Phys.* **1990**, *31*, 27–46.
11. Prasad Reddy, G.V.; Dinesh, P.M.; Sandhya, R.; Laha, K.; Jayakumar, T. Behavior of 321 stainless steel under engineering stress and strain controlled fatigue. *Int. J. Fatigue* **2016**, *92*, 272–280. [\[CrossRef\]](#)
12. Xiao, H.; Cheng, M.; Song, L. Direct fabrication of single-crystal-like structure using quasi-continuous-wave laser additive manufacturing. *J. Mater. Sci. Technol.* **2021**, *60*, 216–221. [\[CrossRef\]](#)
13. Ferré, F.G.; Ormellese, M.; Fonzo, F.D.; Beghi, M.G. Advanced Al₂O₃ coatings for high temperature operation of steels in heavy liquid metals: A preliminary study. *Corros. Sci.* **2013**, *77*, 375–378. [\[CrossRef\]](#)
14. Xu, Z.; Dai, J.; Niu, J.; He, L.; Mu, R.; Wang, Z. Isothermal oxidation and hot corrosion behaviors of diffusion aluminide coatings deposited by chemical vapor deposition. *J. Alloys Compd.* **2015**, *637*, 343–349. [\[CrossRef\]](#)
15. Singh, K.; Fernandes, A.; Paul, B.; Gonal, M.R.; Abraham, G.; Krishnamurthy, N. Preparation and investigation of aluminized coating and subsequent heat treatment on 9Cr–1Mo Grade 91 steel. *Fusion. Eng. Des.* **2014**, *89*, 2534–2544. [\[CrossRef\]](#)
16. Ravi, V.A.; Nguyen, T.K.; Nava, J.C. *Thermochemical Surface Engineering of Steels*; Woodhead Publishing: Sawston, Cambridge, UK, 2015; pp. 751–767.

17. Majumdar, S.; Paul, B.; Kain, V.; Dey, G.K. Formation of Al₂O₃/Fe–Al layers on SS 316 surface by pack aluminizing and heat treatment. *Mater. Chem. Phys.* **2017**, *190*, 31–37. [[CrossRef](#)]
18. Mušálek, R.; Kovářík, O.; Skiba, T.; Haušild, P.; Karlík, M.; Colmenares-Angulo, J. Fatigue properties of Fe–Al intermetallic coatings prepared by plasma spraying. *Intermetallics* **2010**, *18*, 1415–1418. [[CrossRef](#)]
19. Manesh, H.D.; Taheri, A.K. Bond strength and formability of an aluminum-clad steel sheet. *J. Alloys Compd.* **2003**, *361*, 138–143. [[CrossRef](#)]
20. Peng, L.M.; Li, H.; Wang, J.H.; Gong, M. High strength and high fracture toughness ceramic-iron aluminide (Fe₃Al) composites. *Mater. Lett.* **2006**, *60*, 883–887. [[CrossRef](#)]
21. Guu, Y.H.; Hocheng, H. Improvement of fatigue life of electrical discharge machined AISI D2 tool steel by TiN coating. *Mater. Sci. Eng. A* **2001**, *318*, 155–162. [[CrossRef](#)]
22. Poursaiedi, E.; Salarvand, A. Effect of coating surface finishing on fatigue behavior of C450 steel CAPVD coated with (Ti,Cr)N. *J. Mater. Eng. Perform.* **2016**, *25*, 3448–3455. [[CrossRef](#)]
23. Mordyuk, B.N.; Milman, Y.V.; Iefimov, M.O.; Prokopenko, G.I.; Silberschmidt, V.V.; Danylenko, M.I.; Kotko, A.V. Characterization of ultrasonically peened and laser-shock peened surface layers of AISI 321 stainless steel. *Surf. Coat. Technol.* **2008**, *202*, 4875–4883. [[CrossRef](#)]
24. Sealy, M.P.; Guo, Y.B.; Caslaru, R.C.; Sharkins, J.; Feldman, D. Fatigue performance of biodegradable magnesium–calcium alloy processed by laser shock peening for orthopedic implants. *Int. J. Fatigue* **2016**, *82*, 428–436. [[CrossRef](#)]
25. Webster, G.A.; Ezeilo, A.N. Residual stress distributions and their influence on fatigue lifetimes. *Int. J. Fatigue* **2001**, *23*, 375–383. [[CrossRef](#)]
26. Sharafi, S.; Farhang, M.R. Effect of aluminizing on surface microstructure of an HH309 stainless steel. *Surf. Coat. Technol.* **2006**, *200*, 5048–5051. [[CrossRef](#)]
27. Lopez, C.; Kvryan, A.; Kasnakjian, S.; Coronado, A.; Sujittosakul, S.; Villalpando, O.; Ravi, V.A. Effect of austenite stability on pack aluminizing of austenitic stainless steels. *JOM* **2015**, *67*, 61–67. [[CrossRef](#)]
28. Arola, D.; Williams, C.L. Estimating the fatigue stress concentration factor of machined surfaces. *Int. J. Fatigue* **2002**, *24*, 923–930. [[CrossRef](#)]
29. Grosse, M.; Kalkhof, D.; Keller, L.; Schell, N. Influence parameters of martensitic transformation during low cycle fatigue for steel AISI 321. *Phys. B* **2004**, *350*, 102–106. [[CrossRef](#)]
30. Prasad Reddy, G.V.; Sandhya, R.; Sankaran, S.; Mathew, M.D. Low cycle fatigue behavior of 316LN stainless steel alloyed with varying nitrogen content. Part I: Cyclic deformation behavior. *Metall. Mater. Trans. A* **2014**, *45*, 5044–5056. [[CrossRef](#)]
31. Song, W.; Liu, X.; Berto, F.; Razavi, S.M.J. Low-cycle fatigue of 10CrNi3MoV high strength steel and its undermatched welds. *Materials* **2018**, *11*, 661. [[CrossRef](#)]
32. Ye, D.; Matsuoka, S.; Nagashima, N.; Suzuki, N. The low-cycle fatigue, deformation and final fracture behaviour of an austenitic stainless steel. *Mater. Sci. Eng. A* **2006**, *415*, 104–117. [[CrossRef](#)]
33. Branco, R.; Costa, J.D.; Antunes, F.V. Low-cycle fatigue behaviour of 34CrNiMo6 high strength steel. *Theor. Appl. Fract. Mech.* **2012**, *58*, 28–34. [[CrossRef](#)]
34. Stoloff, N.S. Iron aluminides: Present status and future prospects. *Mater. Sci. Eng. A* **1998**, *258*, 1–14. [[CrossRef](#)]
35. Kim, J.K.; Kim, Y.H.; Kim, K.Y. Influence of Cr, C and Ni on intergranular segregation and precipitation in Ti-stabilized stainless steels. *Scr. Mater.* **2010**, *63*, 449–451. [[CrossRef](#)]
36. Schwind, M.; Källqvist, J.; Nilsson, J.O. σ -phase precipitation in stabilization austenitic stainless steels. *Acta Mater.* **2000**, *48*, 2473–2481. [[CrossRef](#)]
37. Kobayashi, S.; Yakou, T. Control of intermetallic compound layers at interface between steel and aluminum by diffusion-treatment. *Mater. Sci. Eng. A* **2002**, *338*, 44–53. [[CrossRef](#)]
38. Peterson, R.E.; Plunkett, R. Stress concentration factors. *Nav. Eng. J.* **1955**, *67*, 697–708. [[CrossRef](#)]
39. Neuber, H. *On the Effect of Stress Concentration in Cosserat Continua*; Springer: Berlin, Germany, 1968; pp. 109–113.
40. Varma, V.K.; Kamat, S.V.; Mahajan, Y.R.; Kutumbarao, V.V. Cyclic stress response of Al–Cu–Mg alloy matrix composites with SiCp of varying sizes. *Scr. Mater.* **1998**, *38*, 1571–1575. [[CrossRef](#)]
41. Kim, K.Y.; Jung, H.G.; Seong, B.G.; Hwang, S.Y. Improvement of cyclic high-temperature corrosion resistance of pack-aluminized heat-resistant stainless steels. *Oxid. Met.* **1994**, *41*, 11–35. [[CrossRef](#)]

42. Lo, K.H.; Shek, C.H.; Lai, J.K.L. Recent developments in stainless steels. *Mater. Sci. Eng. R* **2009**, *65*, 39–104. [[CrossRef](#)]
43. Nam, S.W.; Yoon, Y.C.; Choi, B.G.; Lee, J.M.; Hong, J.W. The normalized Coffin-Manson plot in terms of a new damage function based on grain boundary cavitation under creep-fatigue condition. *Metall. Mater. Trans. A* **1996**, *27*, 1273. [[CrossRef](#)]
44. Tanaka, M.; Miyagawa, O.; Sakaki, T.; Lizuka, H.; Ashihara, F.; Fujishiro, D. Creep rupture strength and grain-boundary sliding in austenitic 21 Cr-4Ni-9Mn steels with serrated grain boundaries. *J. Mater. Sci.* **1988**, *23*, 621–628. [[CrossRef](#)]



© 2020 by the authors. Licensee MDPI, Basel, Switzerland. This article is an open access article distributed under the terms and conditions of the Creative Commons Attribution (CC BY) license (<http://creativecommons.org/licenses/by/4.0/>).